Gated Memristive Coupling in a Hindmarsh–Rose Neural Network: Nonlinear Dynamics and Hardware Implementation

Jiangying Shao(邵降盈)[1], Zhijun Li(李志军)[1*]

1.*School of Automation and Electronic Information, Xiangtan University, Xiangtan, Hunan 41110, China*

Abstract: Inspired by astrocyte-mediated modulation in tripartite synapses, this study proposes a gated memristive coupling mechanism for neural networks. Unlike conventional pairwise coupling scheme with predefined interaction strengths, the proposed framework introduces an independent neuronal state to regulate the evolution of the gated memristive element's state variable, forming a dynamic modulation pathway. Through this mechanism, the coupling strength between two neurons can be continuously adjusted by the activity of a third neuron without directly modifying the intrinsic coupling coefficients. A three-neuron Hindmarsh–Rose network with gated memristive coupling channels is constructed to investigate the resulting nonlinear dynamics. Bifurcation analysis, Lyapunov exponents, and two-parameter maps reveal that the proposed architecture generates diverse transitions among periodic, multi-periodic, and chaotic firing regimes. Different coupling channels exhibit distinct regulatory characteristics, and their interaction produces complex distributions of dynamical regions in the parameter space. Furthermore, external excitation analysis demonstrates that neuronal inputs provide an additional control pathway by modulating the membrane potential of the gating neuron, thereby indirectly regulating the effective coupling strength. The feasibility of the proposed mechanism is validated through real-time digital signal processor (DSP) implementation, where hardware-generated trajectories agree well with numerical simulations. This work provides a compact and hardware-realizable framework for studying state-dependent neural coupling regulation and offers a potential approach for adaptive neuromorphic systems.

Keywords: gated memristive coupling mechanism, dynamic modulation, external excitation

PACS: 05.45.–a, 87.19. lg, 87.19.lj.

* Corresponding author. E-mail address: lizhijun@xtu.edu.cn

1 Introduction

Neural systems exhibit abundant neuronal spiking, bursting and oscillatory dynamics across multi-scale temporal and spatial dimensions, which generate sophisticated nonlinear phenomena closely linked to neural information encoding, signal transmission and collective population activity of biological neurons [1–3]. These diverse firing patterns lay the physiological foundation for sensory processing, memory formation and motor regulation, so revealing the underlying regulatory mechanisms of neuronal dynamics is critical to uncover the operating rules of biological neural computation [4–6]. To quantitatively reproduce and analyze complex firing behaviors, a series of mathematical neuron models have been proposed over the past decades. Among them, the Hindmarsh–Rose (HR) neuron model stands out owing to its concise mathematical structure and powerful capability to replicate typical neuronal activities including regular spiking, multi-period bursting and chaotic oscillation [7,8]. Consequently, the HR framework has become a mainstream tool for investigating neuronal excitability, bifurcation evolution and collective dynamics in coupled neural networks.

In real biological nervous systems, neuronal firing dynamics are not merely governed by intrinsic membrane characteristics of single neurons; inter-neuron coupling interactions serve as a dominant factor in reshaping network collective behaviors. Different synaptic coupling architectures can trigger drastic transitions between periodic, multi-periodic and chaotic firing modes, and further determine the overall dynamical states of neural assemblies [9–12]. For this reason, exploring novel synaptic coupling mechanisms and their induced nonlinear dynamics has become a core research direction in the field of coupled neural networks.

Conventional synaptic transmission was once regarded as a binary interaction solely between presynaptic and postsynaptic neurons. However, the discovery of tripartite synapses has fundamentally updated this classical understanding. Astrocytes, a major subtype of glial cells, actively participate in synaptic modulation and neural information processing [13,14]. Astrocytes can sense electrical signals from adjacent neurons and release gliotransmitters to regulate synaptic efficacy through feedback mechanisms, and this regulatory process carries prominent features including state dependence, slow temporal variation and memory retention, which are primarily mediated by intracellular calcium (Ca^{2+}) concentration dynamics within astrocytes [15]. Such biological evidence indicates that synaptic coupling strength between two neurons is not fixed, but dynamically modulated by a glial state outside the pre–post neuron pair, which provides a core biological inspiration for the modeling work of this paper.

Against the background of synaptic adaptive regulation, memristive coupling has attracted extensive research attention due to its inherent memory characteristics and state-dependent memductance [16–18]. By introducing history-dependent memory effects into synaptic connections, memristive synapses can well mimic biological adaptive synaptic plasticity and enrich the dynamical diversity of neural networks. Numerous existing studies [19–21] have verified that memristive coupling can induce abundant firing mode transitions under different parameter combinations, making memristive neural networks a promising paradigm for modeling biological adaptive neural dynamics.

Despite the fruitful progress of memristive neuron models, most reported memristive coupling architectures are limited to pairwise interaction frameworks [22–24]. In these pairwise models, the time-varying coupling conductance is only controlled by the membrane potential states of the two coupled neurons, while ignoring the regulatory role of astrocytes as an additional modulatory component in tripartite synapses. From a biological perspective, such pairwise coupling structures cannot reproduce the glia-mediated indirect modulation pathway between neurons. Furthermore, existing tripartite synapse models usually introduce complex high-dimensional calcium kinetic equations to characterize astrocytic activities, which results in excessive model complexity and limits hardware implementation. To date, few studies have constructed a lightweight, hardware-friendly neural network model that integrates third-neuron-mediated gating of memristive coupling, and the unique dynamical effects brought by this gating mechanism remain insufficiently explored.

Motivated by the glial modulation mechanism of tripartite synapses, this paper constructs a three-neuron ring Hindmarsh–Rose neural network equipped with bidirectional gated memristive coupling. In the proposed framework, the membrane potential of a third neuron acts as a functional substitute for astrocytic activity, driving the state variable of the proposed gated memristive element to generate time-varying effective coupling weights between the other two neurons. Instead of constant synaptic coefficients in traditional coupling models, the bidirectional interaction strength between each neuron pair is dynamically modulated by the state of a third neuron, forming a minimal network motif that abstracts tripartite synaptic modulation. Furthermore, the proposed architecture introduces an additional external controllability pathway. Neuronal inputs serve not only as drivers of intrinsic firing activity but also as external regulators of inter-neuronal interactions.

Comprehensive numerical simulations and hardware experiments demonstrate that the proposed gated memristive coupling mechanism enables flexible regulation of neuronal dynamics, leading to transitions among periodic, multi-periodic, and chaotic firing regimes through state-dependent modulation of effective coupling strengths. The three memristive coupling channels exhibit distinct regulatory characteristics, and their synergistic interactions determine the distribution of periodic and chaotic regions in the parameter space. Furthermore, external excitation analysis reveals that neuronal inputs can provide an additional control pathway by modulating the membrane potential of the gating neuron, thereby indirectly regulating the effective coupling strengths. Moreover, a real-time digital signal processor (DSP) hardware platform is built to physically implement the proposed network, and experimental oscilloscope trajectories match numerical simulation results well, verifying the hardware feasibility of the gated memristive element modulation mechanism.

The main contributions of this paper are summarized into four aspects as follows:

(1) This paper proposes a novel three-neuron HR network with gated memristive coupling. This lightweight model abstracts the essential glia-mediated regulatory mechanism of tripartite synapses and provides a concise, hardware-implementable framework for exploring state-dependent synaptic modulation in neural dynamics.

(2) A coupling mechanism governed by the state of a third neuron is established, where neuronal activity drives the state variable of the gated memristive element to generate time-varying effective coupling weights through the modulation pathway $x_k \rightarrow \phi_{ij} \rightarrow K_{ij}^{eff}$. The proposed mechanism enables dynamic regulation of inter-neuronal interactions without

directly modifying the intrinsic coupling coefficients, while preserving bidirectional information exchange between coupled neurons.

(3) Comprehensive nonlinear dynamical analyses, including bifurcation diagrams, Lyapunov exponent spectra, phase portraits, time series, and two-parameter dynamical maps, are performed. The results demonstrate that different coupling channels exhibit distinct regulatory effects. Furthermore, external excitation analysis reveals an additional controllability pathway, where neuronal inputs indirectly regulate effective coupling strengths through the gating mechanism, enabling flexible modulation of network dynamics without directly changing the intrinsic coupling coefficients.

(4) A DSP real-time hardware system is established to reproduce the full-range firing behaviors of the proposed model. The consistency between hardware measurement data and numerical simulations confirms the hardware feasibility of the proposed gated memristive coupling network.

The remainder of this paper is organized as follows. Section 2 elaborates the mathematical model and hysteresis characteristics of the gated memristive element. Section 3 establishes the three-neuron HR network with gated memristive coupling and formulates the corresponding dynamic equations. The proposed coupling architecture and state-dependent regulation mechanism are introduced in detail. Section 4 systematically investigates the nonlinear dynamical behaviors of the proposed network, including the effects of individual coupling parameters, their synergistic interactions, and external excitation-induced regulation through the gating pathway. Section 5 introduces the construction of the DSP experimental platform and compares experimental hardware results with numerical simulations. Finally, Section 6 concludes the whole work and discusses future research directions.

2 Gated Memristive Element

This section presents a novel gated memristive element serving as the core gating unit for neural coupling. Unlike conventional two-terminal memristors only regulated by terminal voltage or current [17], the proposed element introduces an independent gating terminal to externally adjust its internal state variable. This design mimics the indirect regulatory pathway of astrocytes in tripartite synapses, where glial signals indirectly modulate synaptic efficacy rather than directly generating postsynaptic currents [25]. We first present the complete mathematical formulation of the gated memristive element, then analyze its hysteresis behavior, and finally characterize its pinched hysteresis fingerprints under electrical excitation and external gating signals.

2.1 Gated Memristive Element Model

Standard two-terminal memristors evolve their internal state variables solely in response to the terminal voltage or current, making them incapable of reproducing the indirect modulation observed in tripartite synapses. To emulate the glia-mediated state-dependent gating effect, the proposed gated memristive element incorporates an independent gating terminal through which its internal state variable is regulated by an external gating signal. The complete voltage-current relation and state evolution equation of the proposed gated memristive element are defined as

$$\begin{cases} i = W(\phi)v \\ \dot{\phi} = \beta v_c - \alpha\phi \end{cases} \tag{1}$$

where v and i represent the input voltage and output current of the gated memristive element, respectively; ϕ is the internal state variable; and v_c is an independent gating signal, which corresponds to the membrane potential of the regulating neuron in the subsequent three-neuron network. The memductance function is defined as $W(\phi) = \alpha+\beta\cos(\phi)$, where α and β represent the baseline memductance and modulation amplitude, respectively, together determining the tunable range of $W(\phi)$. To simplify the model and achieve bidirectional modulation of the coupling strength, we set $\alpha = 0$ and $\beta=1$, yielding $W(\phi) = \cos(\phi)$. A is the gating-signal gain coefficient quantifying the influence of the gating signal, and B is the state relaxation coefficient. By normalizing the parameters such that $A=B=1$, the simplified state equation reduces to $\dot{\phi}=v_c-\phi$.

The fundamental distinction from traditional memristors lies in the state evolution mechanism: the internal state ϕ is completely independent of the main electrical port voltage v and is determined solely by v_c. The port voltage participates only in calculating the output current via the memductance $W(\phi)$, forming a cascaded modulation: $v_c\rightarrow\phi\rightarrow W(\phi)\rightarrow i$. This hierarchical structure captures the essential regulatory logic of tripartite synapses [26]: astrocytes first sense neuronal activity via v_c, integrate signals over time through calcium dynamics (ϕ), and finally feedback to adjust synaptic transmission efficiency ($W(\phi)$).

2.2 Dynamic Gating Mechanism

The gating signal v_c acts as an indirect regulatory input and does not directly contribute to the output current i. Its cascaded regulatory path endows the gated memristive network with inherent memory and phase-lag characteristics.

To intuitively reveal the dynamic response relationship, we apply a sinusoidal gating signal $v_c(t) = A_c\sin(2\pi F_c t)$ and track the time-domain evolution of $v_c(t)$, internal state $\phi(t)$, and memductance $W(\phi(t))$, as illustrated in Fig.1(a). Two typical features can be observed: (1) obvious phase lag exists between $\phi(t)$ and the driving signal $v_c(t)$. The internal state cannot instantaneously follow the change of $v_c(t)$, which originates from the dynamic evolution described by the state equation $\dot{\phi}=v_c(t)-\phi$ and reflects the memory-like effect associated with astrocytic calcium accumulation; (2) the memductance $W(\phi)$ is a nonlinear cosine mapping of ϕ, rather than a direct function of v_c. Even if $v_c(t)$ returns to the same instantaneous value at different time instants, the accumulated $\phi(t)$ differs, leading to distinct memductance values.

Fig.1(b) further plots the parametric trajectory of $v_c(t)$ versus $W(\phi(t))$. The trajectory forms a closed hysteresis loop instead of a single-valued curve, which is a typical signature of history-dependent modulation. The memductance not only depends on the instantaneous value of the gating signal but also retains information about its historical variation process. This hysteretic input–output relationship demonstrates that the proposed gated memristive element can transform a gating signal generated by a third neuron into a time-varying, memory-dependent memductance, thereby providing a modeling basis for state-gated synaptic coupling between neurons.

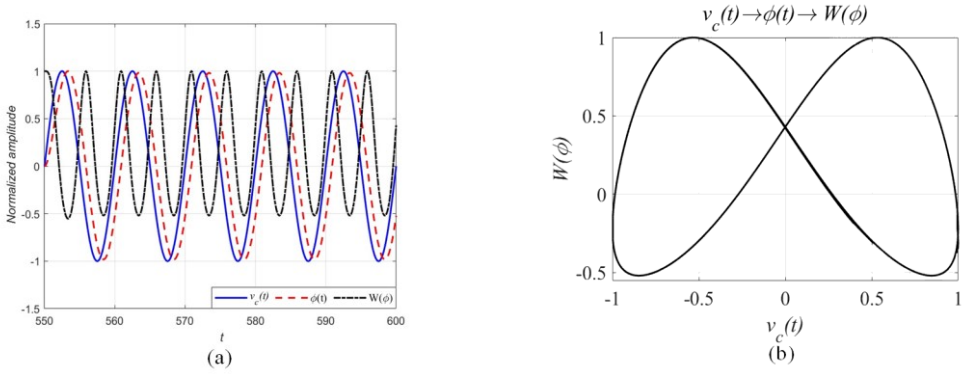


Fig.1. Dynamic responses and input–output characteristics of the proposed gated memristive element. (*a*) Time evolutions of the gating signal $v_c(t)$, the internal state variable $\phi(t)$, and the corresponding memductance $W(\phi)$. (*b*) Hysteretic input–output relationship between $v_c(t)$ and $W(\phi)$.

2.3 Pinched Hysteresis Fingerprints of the Gated Memristive Element

A standard memristor is characterized by a pinched hysteresis loop passing through the origin in its *v*–*i* characteristic curve [23], which serves as the fundamental fingerprint of memristive devices. In this subsection, we verify that the proposed gated memristive element retains this fundamental memristive characteristic. A sinusoidal excitation voltage is applied to the main terminal $v(t) = A\sin(2\pi Ft)$, where A denotes excitation amplitude and F represents excitation frequency. Meanwhile, an independent sinusoidal gating signal $v_c(t) = A_c\sin(2\pi F_c t)$, is applied through the gating terminal. The initial state is set to $\phi(0) = 0$. Two groups of comparative tests are conducted to investigate the effects of excitation amplitude and frequency on the *v*−*i* hysteresis loops. During the frequency analysis, the excitation frequency of the main terminal and that of the gating signal are varied synchronously to maintain consistent dynamic time scales.

Fig.2(a) compares the hysteresis loops under different excitation amplitudes A when F=0.2. All trajectories pass through the origin, exhibiting the characteristic pinched hysteresis of a memristive device. As the excitation amplitude increases, the voltage and current ranges expand simultaneously, and the enclosed hysteresis area becomes larger. A higher excitation amplitude enlarges the output-current range under the same memductance variation, thereby enhancing the observable nonlinear hysteresis behavior. Fig.2(b) illustrates the frequency-dependent hysteresis characteristics with the excitation amplitude fixed at A=5. As the excitation frequency increases, the response speed of the internal state gradually lags behind the excitation signal, causing the hysteresis loop to shrink. At low frequencies, the internal state has sufficient time to evolve within each excitation cycle, resulting in a broad hysteresis loop. As the frequency increases, the state variable cannot fully evolve during one cycle, leading to a contraction of the hysteresis region. This frequency-dependent behavior demonstrates that the proposed gated memristive element exhibits the characteristic dynamic hysteresis response of memristive devices.

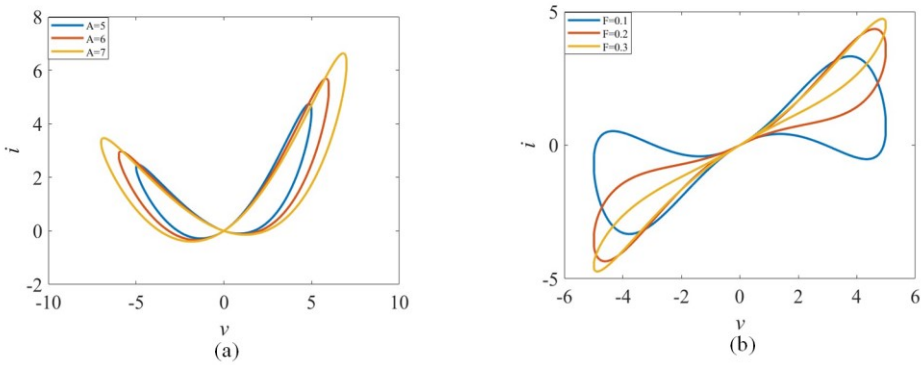


Fig. 2. Voltage–current hysteresis characteristics of the proposed gated memristive element (a) Amplitude-dependent hysteresis loop with A_c =2, F_c =0.1 and frequency F = 0.2 fixed. (b) Frequency-dependent hysteresis loop with A_c=2 and A=5 fixed.

3 Gated Memristive Neural Coupling Architecture

3.1 Original Two-Dimensional Hindmarsh–Rose Neuron Model

First, we briefly introduce the classic 2D Hindmarsh–Rose (HR) neuron proposed in 1982 [27], which can reproduce spiking and bursting behaviors with simple mathematical expressions. The standard single HR neuron is governed by

$$\begin{cases} \dfrac{dx}{dt} = y - ax^3 + bx^2 + I \\ \dfrac{dy}{dt} = c - dx^2 - y \end{cases} \tag{2}$$

wherein two variables x and y are the membrane potential and recovery variable, respectively, and I stands for the external input current. The parameters a, b, c, and d are four positive constants, which are often fixed as a = 1, b = 3, c = 1, d = 5.

This minimal neuron model serves as the basic unit for constructing the proposed multi-neuron network. All three neurons in the ring network follow identical HR intrinsic dynamics, and their mutual interactions are realized through gated memristive coupling governed by the state of a third neuron. This coupling architecture captures the essential glia-mediated regulatory mechanism underlying tripartite synapses [28].

3.2 Topology of the Three-Neuron Gated Memristive Coupling Network

Inspired by tripartite synapses [29], we design a closed ring network containing three HR neurons (Neuron 1, Neuron 2, Neuron 3) with three bidirectional memristive coupling channels. Unlike conventional pairwise coupling, each coupling channel is modulated by a third-party neuron outside the coupled pair, forming a full tripartite regulatory loop. The coupling channel between Neuron 1 and Neuron 2 is gated by the membrane potential x_3 of Neuron 3; the coupling channel between Neuron 2 and Neuron 3 is gated by the membrane potential x_1 of Neuron 1, and the coupling channel between Neuron 3 and Neuron 1 is gated by the membrane potential x_2 of Neuron 2. Fig.3 illustrates the network topological structure. Each gated memristive element sits between two neurons, and a directed auxiliary signal path delivers the membrane potential of the third neuron to regulate the internal state variable of the gated memristive element. This design breaks the limitation of traditional fixed coupling

and pairwise memristive coupling, providing a minimal mathematical prototype to study glia-mediated state-dependent synaptic modulation. As summarized in Table 1, each pairwise coupling channel is governed by a standardized three-stage modulation chain.

Table 1. Third-neuron-state-gated coupling relationships in the proposed network

Coupling channel	third-neuron state	Gating variable	Effective coupling weight	Modulation pathway
1-2	$x_3(t)$	$\phi_{12}(t)$	$K_{12}^{eff}(t)=k_{12}\cos(\phi_{12}(t))$	$x_3(t)\rightarrow\phi_{12}(t)\rightarrow K_{12}^{eff}$
2-3	$x_1(t)$	$\phi_{23}(t)$	$K_{23}^{eff}(t)=k_{23}\cos(\phi_{23}(t))$	$x_1(t)\rightarrow\phi_{23}(t)\rightarrow K_{23}^{eff}$
3-1	$x_2(t)$	$\phi_{31}(t)$	$K_{31}^{eff}(t)=k_{31}\cos(\phi_{31}(t))$	$x_2(t)\rightarrow\phi_{31}(t)\rightarrow K_{31}^{eff}$

3.3 Full Mathematical Formulation of the Three-Neuron Network

Combining the HR neuron prototype and the gated memristive element in Section 2, we establish the complete differential equation system for the gated-coupling three-neuron network. The whole system can be described as:

$$\begin{cases} \dot{x}_1 = x_1^3 + bx_1^2 + I_1 + k_{12}\cos(\phi_{12})(x_2 - x_1) + k_{31}\cos(\phi_{31})(x_3 - x_1) \\ \dot{y}_1 = x_1^2 - y_1 \\ \dot{x}_2 = x_2^3 + bx_2^2 + I_2 + k_{12}\cos(\phi_{12})(x_1 - x_2) + k_{23}\cos(\phi_{23})(x_3 - x_2) \\ \dot{y}_2 = x_2^2 - y_2 \\ \dot{x}_3 = x_3^3 + bx_3^2 + I_3 + k_{23}\cos(\phi_{23})(x_2 - x_3) + k_{31}\cos(\phi_{31})(x_1 - x_3) \\ \dot{y}_3 = c - dx_3^2 - y_3 \\ \dot{\phi}_{12} = \\ \dot{\phi}_{23} = \\ \dot{\phi}_{31} = \end{cases} \tag{3}$$

Variables ϕ_{12}, ϕ_{23} and ϕ_{31} denote the internal state variables of the gated memristive elements for the coupling channels between neuron pairs 1–2, 2–3 and 3–1, respectively. $K_{ij}^{eff} = k_{ij}\cos(\phi_{ij})$ represents the time-varying effective coupling weight of channel i–j, which replaces the constant synaptic weight in traditional coupling models.

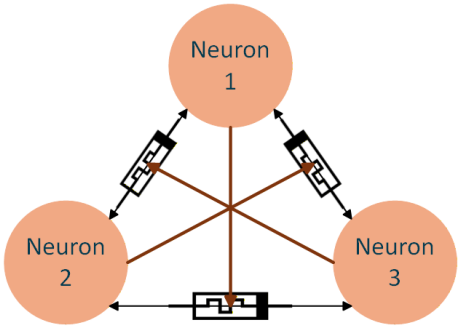


Fig.3. Three-neuron HR network with gated memristive coupling

It should be clarified that our model serves as a functional abstraction of tripartite synaptic modulation rather than a detailed biochemical calcium model. The clear one-to-one conceptual correspondence is outlined as follows:

1. Paired HR neurons (Neuron i and Neuron j): Functionally analogous to pre-synaptic and post-synaptic neurons forming the basic synaptic connection.

2. Third regulatory neuron (Neuron k): Serves as a reduced-order functional analogue of astrocytes, which senses the surrounding neuronal electrical activity.
3. Internal state variable ϕ_{ij}: Captures the slow accumulation and history-dependent modulation features, conceptually mirroring the temporal integration process associated with astrocytic calcium signaling.
4. Time-varying effective coupling weight $k_{ij}\cos(\phi_{ij})$: Emulates the feedback regulation of synaptic efficacy via gliotransmitters released by astrocytes, where the cosine memductance function provides bidirectional modulation (positive/negative) of the coupling strength.

Compared with conventional tripartite synapse models that incorporate multiple high-order calcium dynamics, the proposed gated memristive modeling framework substantially reduces model complexity and computational cost. This low-complexity design makes the network particularly suitable for real-time digital hardware platforms such as DSPs, as will be verified in Section 5, while still retaining the core dynamical feature of state-dependent synaptic gating.

4 Neuronal dynamics analysis

This section systematically explores how the three core baseline coupling coefficients k_{12}, k_{23}, and k_{31} regulate the spiking, periodic and chaotic firing behaviors of the three-neuron gated memristive HR network. Each parameter corresponds to the base modulation strength of one ring coupling channel, and the final effective synaptic weight $K_{ij}^{eff} = k_{ij}\cos(\phi_{ij})$ is jointly determined by the baseline coefficient and the internal state variable of the gated memristive element regulated by the third neuron. In the following analysis, the system parameters are fixed as $a = 1$, $b = 3$, $c = 1$, $d = 5$, $I_1 = 0.5$, $I_2 = 0.1$, $I_3 = 0.3$, and initial states of all variables are fixed as 0. The ODE45 algorithm is adopted to solve the differential system with time step $\Delta t = 10^{-3}$ and total simulation duration $T = 1000$. Transient data in the first 500 time units are discarded to eliminate initial transient responses, and only steady-state asymptotic trajectories are retained for analysis. The Wolf algorithm is utilized to calculate Lyapunov exponent (LE) spectra to quantitatively distinguish periodic, multi-periodic and chaotic states [30].

4.1 Individual regulatory effect of coupling strength k_{12}

To reveal the regulatory effect of k_{12}, we fix the other two coupling strengths as $k_{23} = 0.4$, $k_{31} = 0.5$, and scan k_{12} within the range [1, 2]. The parameter interval is selected after preliminary wide-range scanning. This window fully contains the complete state transition from single-period oscillation to chaos via period-doubling bifurcations.

Fig.4(a) shows the bifurcation diagram of membrane potential x_1 with respect to k_{12}, and Fig. 4(b) plots the corresponding three-dimensional Lyapunov exponent spectrum. With the gradual increase of k_{12}, the system undergoes a clear monotonic evolution. When $k_{12} < 1.15$, the maximum Lyapunov exponent $LE_1=0$ and the remaining LEs are negative, corresponding to a stable period-1 limit cycle. As k_{12} rises, period-doubling bifurcations emerge continuously, forming a cascade of multi-periodic firing windows. When k_{12} exceeds a critical threshold near 1.8, $LE_1>0$, indicating the system enters a sustained chaotic firing regime.

Fig. 5 further displays representative phase portraits (x–y plane) and membrane potential time series under three typical k_{12} values. At $k_{12} = 1.0$ (Figs.5(a) and (b)), the phase portrait forms a single, simple closed loop, accompanied by a perfectly periodic time series, indicative of period-1 firing. When $k_{12} = 1.3$ (Figs. 5(c) and (d)), the attractor evolves into a distinct

double-loop structure, and the oscillation amplitude alternates regularly between two levels, confirming a period-2 firing state. At k_{12} = 2 (Figs.5(e) and (f)), the phase portrait further develops into a complex, fractal-like structure, while the time series becomes aperiodic and erratic, indicating the emergence of chaotic firing.

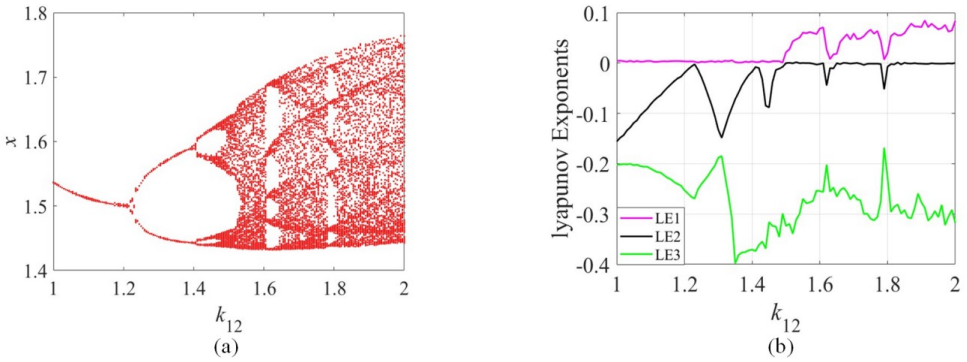


Fig. 4. The neuronal ring network exhibits dynamic evolution that changes over the range $k_{12} \in [1, 2]$, with $k_{23} = 0.4$ and $k_{31} = 0.5$ fixed. (a) bifurcation diagram. (b) Lyapunov exponent diagram.

The parameter k_{12} determines the modulation scale of the effective coupling weight $K_{12}^{eff} = k_{12}\cos(\phi_{12}(t))$. Therefore, increasing k_{12} strengthens the state-dependent interaction between Neurons 1 and 2, rather than merely increasing a constant pairwise coupling. Since the gating variable ϕ_{12} is driven by the membrane potential x_3 of Neuron 3, the 1–2 coupling channel forms part of a closed feedback pathway: the state of Neuron 3 regulates the interaction between Neurons 1 and 2, while the resulting changes in x_1 and x_2 are transmitted back to Neuron 3 through the remaining coupling channels. Under the parameter setting considered here, increasing k_{12} amplifies the gain of this closed-loop interaction. As a result, the original period-1 orbit gradually loses stability, undergoes successive period-doubling bifurcations, and eventually evolves into chaotic firing. Thus, the complexity-promoting role of k_{12} originates from the amplification of third-neuron-state-dependent feedback within the three-neuron loop.

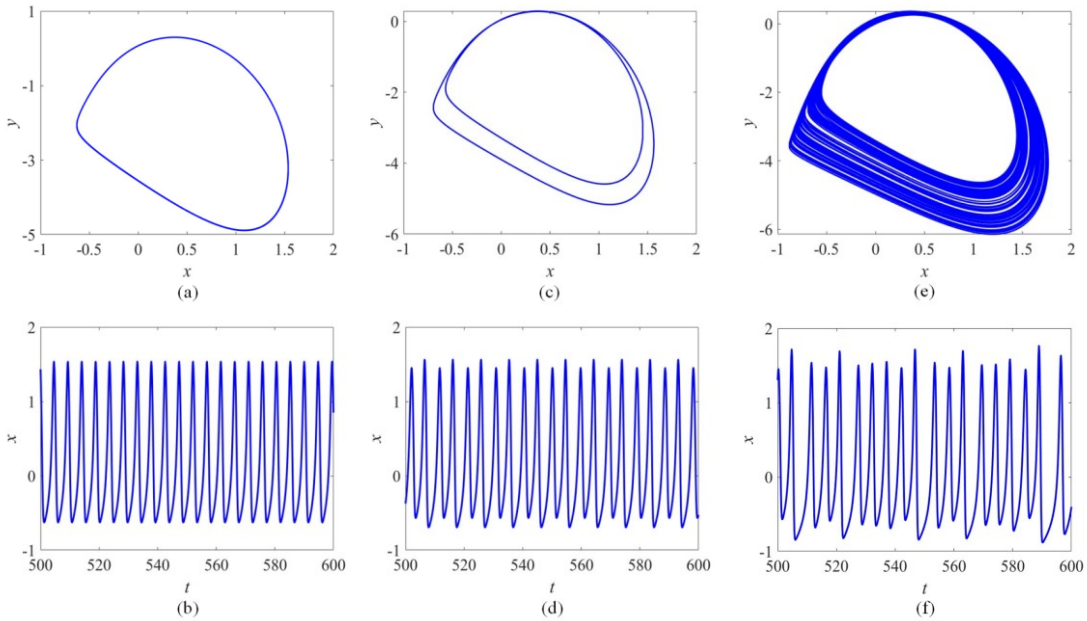


Fig. 5. Representative firing patterns for different values of k_{12}, with k_{23} = 0.4 and k_{31} = 0.5 fixed. The upper panels show phase portraits in the x–y plane, and the lower panels show the corresponding time series of $x(t)$. (a) and (b) period-1 firing at k_{12} = 1.0. (c) and (d) period-2 firing at k_{12} = 1.3. (e) and (f) Chaotic firing at k_{12} = 2.0.

4.2 Individual regulatory effect of coupling strength k_{23}

We fix k_{12} = 0.1, k_{31} =1 and scan $k_{23} \in [0.5,1.5]$. This parameter range covers full transitions from chaotic oscillation to stable single-period firing. The bifurcation diagram (Fig.6(a)) and Lyapunov exponent spectrum (Fig.6(b)) exhibit consistent trends. When $k_{23} < 0.8$, countless scattered and disorganized points can be observed across the whole range of the bifurcation diagram. Meanwhile, the maximum Lyapunov exponent remains positive all the time. Such numerical features clearly indicate that the neuronal network is dominated by chaotic firing behavior under this parameter condition. As k_{23} gradually rises, obvious periodic windows start to emerge within the bifurcation diagram. Accompanied by this structural change, the value of LE_1 decreases and returns to zero.

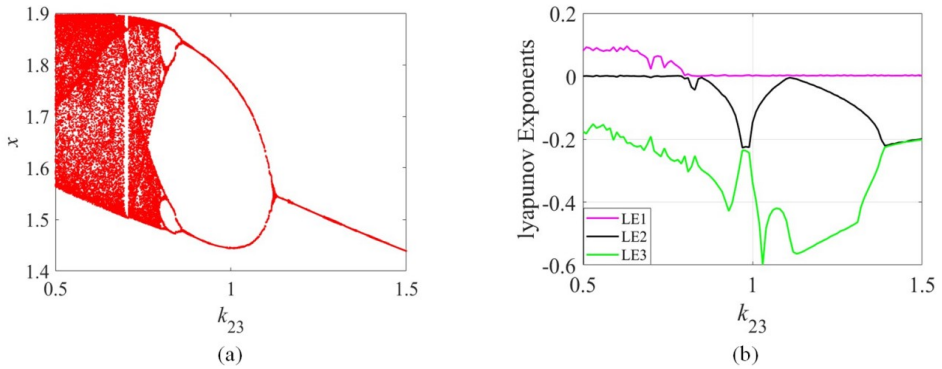


Fig.6. The neuronal ring network exhibits dynamic evolution that changes over the range $k_{23} \in [0.5, 1.5]$, with k_{12} = 0.1 and k_{31} = 1 fixed. (a) bifurcation diagram. (b) Lyapunov exponent diagram.

Fig.7 provides visual evidence of firing pattern transformation under selected k_{23} values. At k_{23}= 0.5, the phase portrait forms a tangled irregular attractor, and the membrane potential

time series fluctuates randomly without fixed spike cycles (Fig.7(a)). At k_{23} = 1.0, two closed orbits appear in the phase plane, and the time series alternates between two spike amplitudes at fixed time intervals (Fig.7(b)). At k_{23} = 1.5, the phase space only holds one simple closed loop, and the time series generates uniform, regularly spaced spikes (Fig.7(c)).

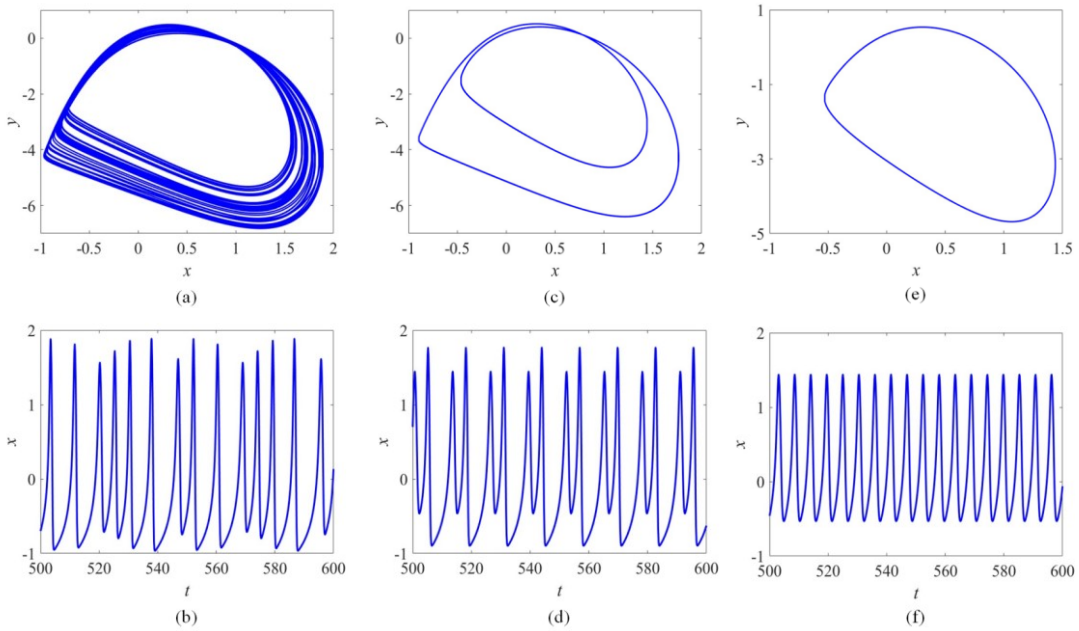


Fig.7. Representative firing patterns for different values of k_{23}, with k_{12} = 0.1 and k_{31} = 1 fixed. The upper panels show phase portraits in the x–y plane, and the lower panels show the corresponding time series of $x(t)$. (a) and (b) Chaotic firing at k_{23} = 0.5. (c) and (d) period-2 firing at k_{23} = 1. (e) and (f) period-1 firing at k_{23} = 1.5.

The distinct role of k_{23} originates from the structural position of the corresponding gated channel within the three-neuron feedback network. Unlike k_{12}, which directly strengthens the interaction between Neurons 1 and 2, the parameter k_{23} regulates the gated information exchange between Neurons 2 and 3 through the effective coupling weight $K_{23}^{eff}(t)$. Since the gating variable ϕ_{23} is controlled by the membrane potential of Neuron 1, increasing k_{23} enhances the influence of Neuron 1 on the interaction between the remaining two neurons. Under the present parameter setting, this additional regulation suppresses the irregular fluctuations circulating within the three-neuron feedback loop and gradually stabilizes the periodic orbit. Consequently, chaotic oscillations are replaced by periodic firing as the closed-loop dynamics become increasingly regular.

4.3 Regulatory Role of the Coupling Strength k_{31}

We fix k_{12} = 1.2 and k_{23} = 0.5, and investigate the regulatory role of k_{31} within the range [0.3, 0.5]. It should be noted that this scanning range is narrower than those adopted for k_{12} and k_{23}. This is because, under the present parameter configuration, k_{31} does not act as a globally dominant coupling parameter that reverses the overall evolutionary trend of the network. Instead, it primarily serves as a boundary-regulating parameter that reshapes the transition between periodic and chaotic firing regimes. The range [0.3, 0.5] is selected because it covers the complete transition from chaotic firing to stable period-1 oscillation under the fixed values of k_{12} = 1.2 and k_{23} = 0.5, which allows the regulatory effect of k_{31} on the periodic–chaotic boundary to be clearly identified.

Fig.8(a) presents the bifurcation diagram with k_{31} as the control parameter, and Fig.8(b) plots the corresponding Lyapunov exponent spectrum. When $k_{31} < 0.39$, the maximum Lyapunov exponent stays positive, and discrete scattered points fill the bifurcation diagram, which means the network operates under fully chaotic spiking mode. When k_{31} increases to 0.43, scattered points reduce significantly, and periodic windows appear in the bifurcation diagram, with the maximum Lyapunov exponent falling back to zero to match period-2 oscillation. When k_{31} reaches 0.45, all scattered branches vanish, and only one stable orbit exists in the bifurcation diagram, accompanied by all non-positive Lyapunov exponents that correspond to stable period-1 firing. These results indicate that, although the effective adjustment range of k_{31} is relatively narrow, it can still clearly shift the system among chaotic, period-2, and period-1 firing states.

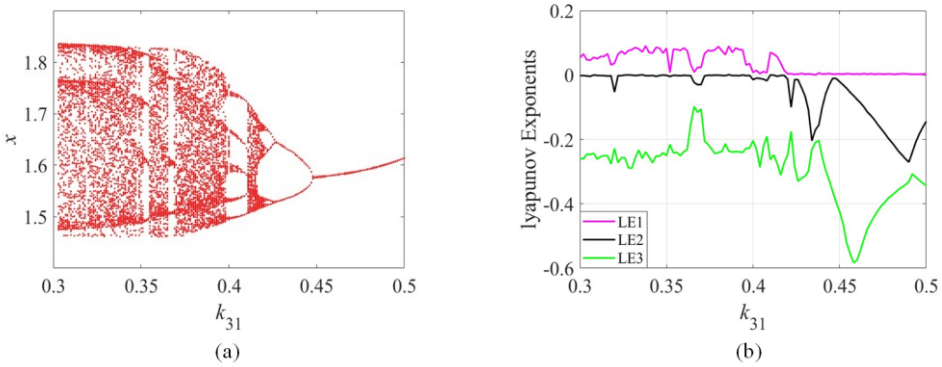


Fig.8 The neuronal ring network exhibits dynamic evolution that changes over the range $k_{31} \in [0.3, 0.5]$, with $k_{12} = 1.2$ and $k_{23} = 0.5$ fixed. (a) bifurcation diagram. (b) Lyapunov exponent diagram.

Fig.9 displays phase portraits and membrane potential time series under three typical k_{31} values, which intuitively reflect the gradual regularization of neuronal firing as k_{31} grows. The narrow effective adjustment range determines that k_{31} can only fine-tune the transition boundary of different dynamical states, instead of dominating the overall evolution trend of the network.

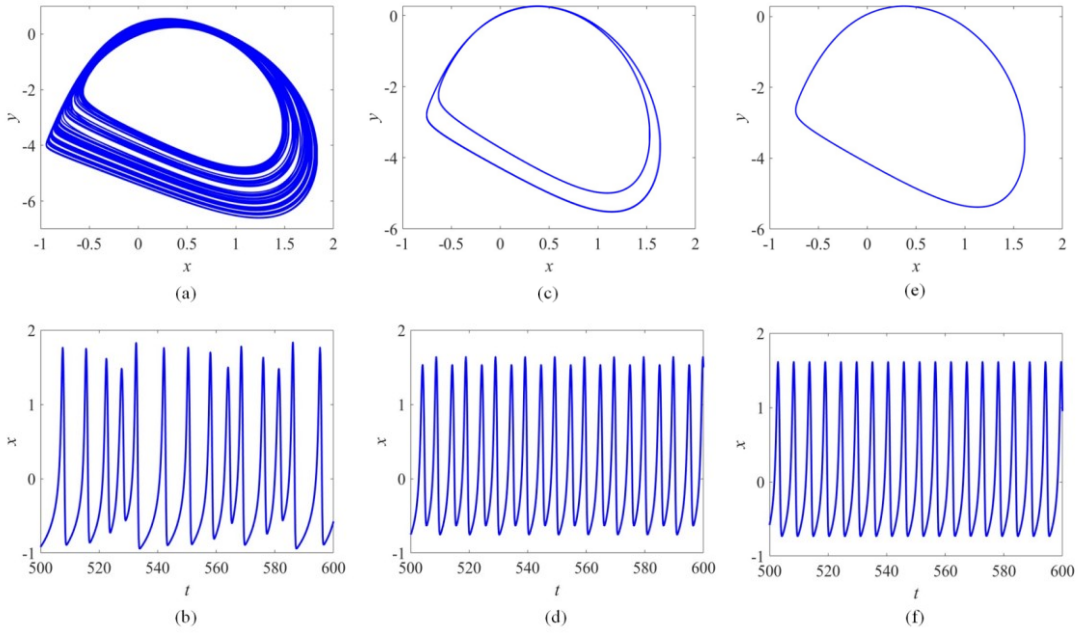


Fig.9 Representative firing patterns for different values of k_{31}, with k_{12} = 1.2 and k_{23} = 0.5 fixed. The upper panels show phase portraits in the x–y plane, and the lower panels show the corresponding time series of $x(t)$. (a) and (b) Chaotic firing at k_{31} = 0.3. (c) and (d) period-2 firing at k_{31} = 0.43. (e) and (f) period-1 firing at k_{31} = 0.5.

The dynamical role of k_{31} differs from those of k_{12} and k_{23} because it regulates a different branch of the third-neuron-mediated gated feedback network. Specifically, the parameter k_{31} determines the modulation scale of the effective coupling weight $K_{31}^{eff}(t)$, which controls the interaction between Neurons 3 and 1 under the gating action of Neuron 2. Consequently, increasing k_{31} does not simply strengthen the interaction between a pair of neurons, but redistributes the feedback balance within the closed three-neuron loop. Under the present parameter setting, the enhanced 3–1 interaction gradually compensates for the irregular fluctuations generated by the remaining feedback branches. As a result, the chaotic attractor progressively loses stability and is replaced by regular periodic oscillations. It should be further emphasized that the relatively narrow range of k_{31} is consistent with its role as a boundary-regulating rather than a globally dominant parameter. Within this range, however, k_{31} still effectively controls the transition among chaotic, period-2, and period-1 firing states. Therefore, the analysis of k_{31} provides a meaningful characterization of how the third gated coupling channel fine-tunes the stability of the network, even though it does not dominate the global parameter-space organization.

4.4 Two-Parameter Dynamical Maps

Single-parameter bifurcation analysis only reflects the independent influence of one coupling coefficient while keeping the other two parameters unchanged. This analysis method cannot capture the mutual restriction or cooperative promotion effects generated when two coupling strengths adjust simultaneously. To draw a full picture of periodic and chaotic state distribution in two-dimensional parameter spaces, we construct three groups of two-parameter dynamical color maps. In all plotted parameter planes, integers from 1 to 15 are used to mark areas with different periodic firing orders, and red regions labeled CH stand for parameter ranges that produce chaotic neuronal firing.

The k_{12}-k_{23} parameter plane illustrates the combined regulation of two third-neuron-mediated feedback pathways associated with Neuron 2. Specifically, k_{12} controls the interaction between Neurons 1 and 2, whereas k_{23} regulates the interaction between Neurons 2 and 3. Since both coupling channels influence the dynamics of Neuron 2, the firing behavior is jointly determined by the variation of these two gated pathways. As shown in Fig.10(a), the blue regions correspond to low-period oscillations, whereas the red regions indicate chaotic firing. Increasing k_{23} generally enlarges the low-period region, while increasing k_{12} tends to extend the high-period and chaotic regions under the investigated parameter range. Near the transition area between periodic and chaotic states, several periodic windows appear, indicating that the stability of the network depends on the balance between these two third-neuron-mediated gated feedback pathways.

Fig.10(b) presents the dynamical distribution in the k_{12}–k_{31} parameter plane. Compared with Fig.10(a), this parameter plane exhibits a more intricate arrangement of different firing regimes, with periodic windows appearing within the surrounding high-period and chaotic regions. This behavior can be attributed to the fact that both k_{12} and k_{31} directly contribute to the membrane-potential equation of Neuron 1 through two independent third-neuron-mediated coupling channels. K_{12}^{eff} is regulated by the state of Neuron 3, whereas

$K_{31}^{eff}(t)$ is controlled by Neuron 2. Consequently, Neuron 1 receives two dynamically modulated inputs originating from different feedback pathways. The simultaneous variation of k_{12} and k_{31} changes the relative influence of these two gated interactions, resulting in a more complex distribution of stability regions in the parameter plane.

Fig.10(c) shows the dynamical distribution in the k_{23}–k_{31} parameter plane. When k_{23} is relatively small, chaotic and high-period regions occupy a larger portion of the parameter space. As k_{23} increases, the low-period region expands, suggesting that the corresponding third-neuron-mediated pathway tends to stabilize the network dynamics under the present parameter conditions. However, further variation of k_{23} together with k_{31} results in the emergence of additional high-period regions, indicating that the stabilizing effect of k_{23} depends on the specific parameter interval. Meanwhile, k_{31} mainly modifies the transition boundaries between different firing regimes through its associated third-neuron-mediated feedback pathway.

The three two-parameter maps reveal that the network dynamics are jointly regulated by multiple coupling channels rather than any single parameter. The (k_{12}-k_{31}) plane exhibits the most complex interwoven periodic-chaotic structures, while the (k_{23}-k_{31}) plane confirms the dominant stabilizing role of k_{23}. These results demonstrate the combined, channel-dependent modulation effects of the proposed gated memristive coupling mechanism.

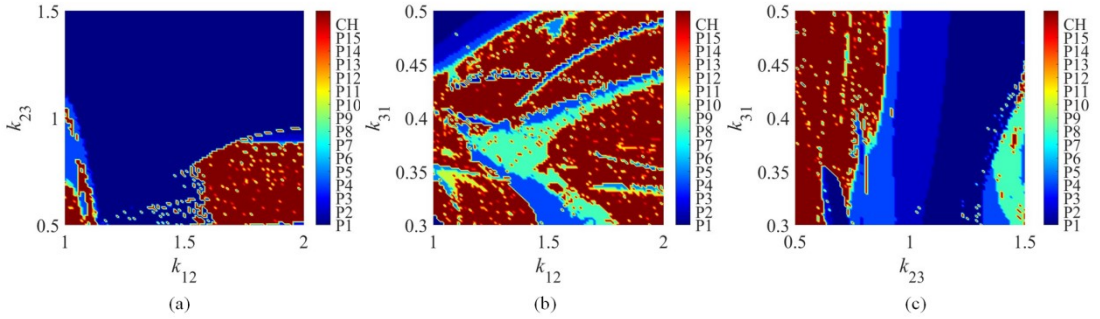


Fig. 10 Two-dimensional dynamic mappings. (a) k_{12}-k_{23} plane with $k_{31}=0.1$. (b) k_{12}-k_{31} plane with $k_{23}=0.4$. (c) k_{23}- k_{31} plane with $k_{12}=0.1$.

4.5. External excitation controlled dynamical regulation through third-party gating

We have already examined the influence of the coupling parameters k_{12}, k_{23}, and k_{31} on network dynamics. However, in the proposed third-neuron-mediated gating architecture, the effective coupling strength is not determined solely by these preset coefficients. Since internal gating variables are driven by neuronal states, external excitatory inputs provide an additional pathway for modulation without directly altering the coupling parameters. Specifically, the external excitation of each neuron establishes an indirect modulation pathway:

$$\begin{aligned} I_1 &\rightarrow x_1 \rightarrow \phi_{23} \rightarrow K_{23}^{eff} \\ I_2 &\rightarrow x_2 \rightarrow \phi_{31} \rightarrow K_{31}^{eff} \\ I_3 &\rightarrow x_3 \rightarrow \phi_{12} \rightarrow K_{12}^{eff} \end{aligned} \tag{4}$$

Through these pathways, the external excitation of each neuron not only affects its intrinsic firing behavior but also dynamically regulates the interaction strength of another coupling channel controlled by this neuron. Therefore, the network dynamics are determined not only

by the fixed coupling coefficients k_{ij}, but also by the activity-dependent modulation introduced mediated by the third neuron.

Fig.11(a) illustrates the bifurcation behavior as I_1 varies, with $I_2 = 0.1$, $I_3 = 0.3$, $k_{12} = 1.3$, $k_{23} = 0.4$, and $k_{31} = 0.5$. Because neuron 1 acts as a third-party controller for the coupling channel between neurons 2 and 3, altering I_1 changes the evolution of x_1, thereby influencing ϕ_{23} and K_{23}^{eff}. Consequently, the observed transitions between different firing states arise from the indirect modulation of the interaction between neurons 2 and 3, rather than from direct changes to the coupling parameters.

Fig.11 (b) shows the bifurcation behavior as I_2 varies, with parameters set to $I_1 = 0.5$, $I_3 = 0.3$, $k_{12} = 0.1$, $k_{23} = 1$, and $k_{31} = 1$. Altering I_2 changes the evolution of x_2 thereby affecting ϕ_{31} and K_{31}^{eff}, demonstrating how the third-neuron-mediated gating mechanism can influence the behavior of the entire network.

Fig.11 (c) presents the bifurcation diagram obtained by varying I_3, with parameters set to $I_1 = 0.5$, $I_2 = 0.1$, $k_{12} = 1.2$, $k_{23} = 0.5$, and $k_{31} = 0.43$. Neuron 3 acts as a third-party regulator for the coupling channel between neurons 1 and 2; thus, external excitation applied to neuron 3 indirectly alters the effective coupling weight K_{12}^{eff}. The resulting changes in firing patterns indicate that the activity of an auxiliary neuron can serve as an external control source to modulate interactions between other neurons.

These results demonstrate that the proposed third-neuron-mediated gated coupling mechanism introduces an additional controllability pathway beyond conventional coupling systems.

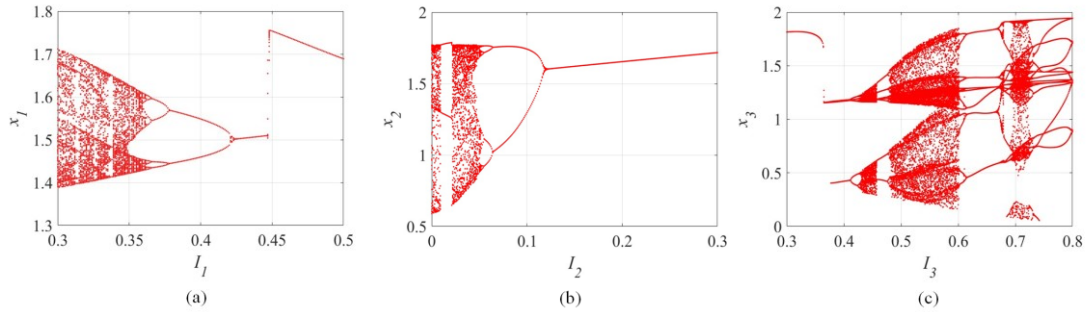


Fig. 11. Bifurcation diagrams under different external stimuli. (a) Dynamic response of x_1 versus I_1 with $I_2 = 0.1$, $I_3 = 0.3$, $k_{12} = 1.3$, $k_{23} = 0.4$, and $k_{31} = 0.5$. (b) Dynamic response of x_2 versus I_2 with $I_1 = 0.5$, I_3=0.3, $k_{12} = 0.1$, $k_{23} = 1$, and k_{31}=1. (c) Dynamic response of x_3 versus I_3 with $I_1 = 0.5$, $I_2 = 0.1$, $k_{12} = 1.2$, $k_{23} = 0.5$, and $k_{31} = 0.43$, demonstrating the regulation of neuronal firing states via third-party stimulation.

5 DSP-Based Experimental Verification

To validate the hardware realizability and real-time operational capability of the proposed bidirectional third-neuron-state-dependent gated memristive neural network, we implement the numerical model on a real-time digital hardware platform. Digital signal processors (DSPs) have been widely adopted for hardware realization of nonlinear dynamical systems, chaotic circuits, and neural network models, owing to their high-speed floating-point computation, robust real-time processing performance, and excellent numerical stability [31,32]. In this work, we employ a DSP-based implementation to reproduce the dynamical behaviors

of the proposed network and experimentally verify the effectiveness of the gated memristive coupling mechanism.

The hardware architecture of the real-time DSP platform is illustrated in the block diagram of Fig.12. The core of the system is a 32-bit floating-point DSP chip, TMS320F28335, which performs real-time numerical integration of the coupled differential equations governing the bidirectional gated neural model, as given in Eq. (3). At each time step, the iterative solver updates the state variables, gating variables, and the associated gated coupling terms, thereby realizing the bidirectional state-dependent coupling mechanism in hardware. The computed state variables are then mapped to digital output values and converted into analog voltage signals via a dual-channel 16-bit digital-to-analog converter (DAC8552). These analog outputs are visualized on a digital oscilloscope (Tektronix MSO 3032), allowing direct observation of the dynamic behaviors and attractors of the gated coupling system. Program downloading and debugging are accomplished through a TI XDS100v1 USB emulator, with the integrated development environment Code Composer Studio.

Before the computational program is transferred to the DSP, several initialization steps are carried out, including system-clock configuration, DAC initialization, timer-interrupt configuration, and memory allocation for the system states and model parameters. The coupled differential equations are solved in real time using the fourth-order Runge–Kutta (RK4) scheme. A fixed integration step of (h=0.001) is employed, consistent with the step size used in the numerical simulations. During each interrupt cycle, the state variables and gated coupling terms are updated according to the RK4 scheme, after which the calculated states are appropriately scaled and transferred to the DAC for analog output.

A photograph of the physical hardware setup is shown in Fig. 13. To accommodate the output voltage range of the DSP platform (−5 V to +5 V), the state variables generated by the neural network are linearly scaled prior to transmission to the DAC. Representative experimental time series and phase portraits obtained from the DSP platform are presented in Figs. 13-15 for different gated coupling strength settings.

Fig.14 presents the experimental results for varying k_{12}, with k_{23} = 0.4 and k_{31} = 0.5 fixed. The upper panels display phase portraits in the x–y plane, and the lower panels show the corresponding time series of $x(t)$. Figs.14(a) and (b) correspond to period-1 firing at k_{12}=1.0; Figs. 14(c) and (d) show period-2 firing at k_{12} = 1.3; and Figs. 14(e) and (f) present chaotic firing at k_{12} = 2.0.

Fig.15 shows the experimental results for varying k_{23}, with k_{12} = 0.1 and k_{31} = 1 fixed. Chaotic firing at k_{23} = 0.5 is shown in Figs. 15(a) and (b); period-2 firing at k_{23} = 1.0 in Figs. 15(c) and (d); and period-1 firing at k_{23} = 1.5 in Figs. 15(e) and (f).

Fig.16 depicts the experimental results for varying k_{31}, with k_{12} = 1.2 and k_{23} = 0.5 fixed. Chaotic firing at k_{31} = 0.3 is shown in Figs. 16(a) and (b); period-2 firing at k_{31} = 0.43 in Figs. 16(c) and (d); and period-1 firing at k_{31} = 0.5 in Figs. 16(e) and (f).

Overall, the experimentally measured time series and phase portraits are in excellent agreement with their numerical simulation counterparts presented in Section 4. The hardware-generated trajectories successfully reproduce the main dynamical characteristics predicted by the numerical simulations across all three coupling channels. Although minor discrepancies inevitably arise from finite sampling precision, DAC quantization error, and hardware noise, the overall topological structures and oscillatory behaviors remain highly

consistent with the simulation results. This strong agreement demonstrates that the proposed bidirectional third-neuron-mediated gated memristive neural network can be effectively implemented on a real-time DSP platform, verifying its hardware feasibility and practical realization.

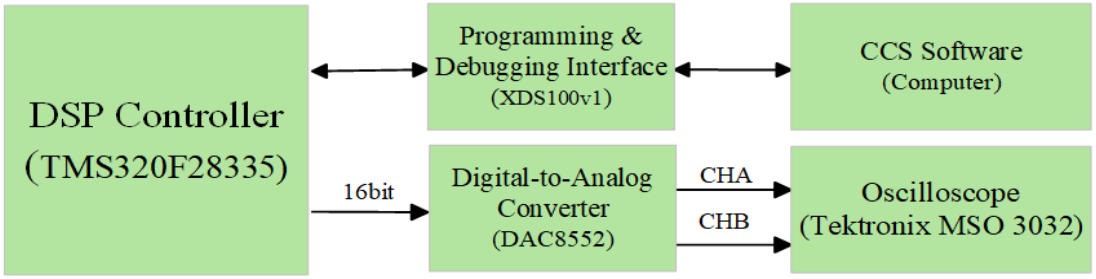


Fig.12. Block diagram of the DSP-based experimental platform.

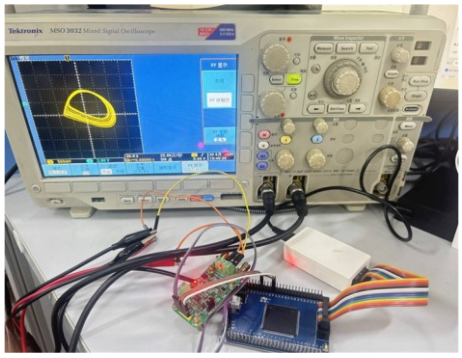


Fig.13. Photograph of the DSP-based experimental platform.

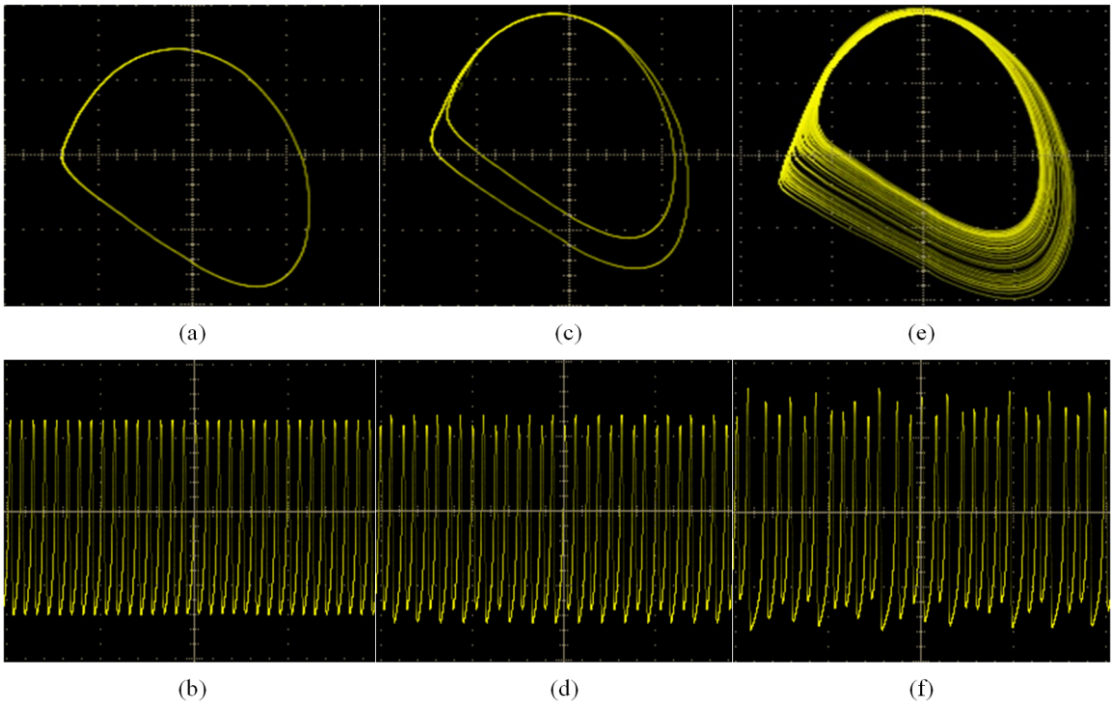


Fig. 14. Experimental time series and phase portraits obtained from the DSP platform for different values of k_{12}, with $k_{23} = 0.4$ and $k_{31} = 0.5$ fixed. The upper panels show phase portraits in the x–y plane, and the lower panels show the corresponding time series of $x(t)$. (a) and (b) $k_{12} = 1$. (c) and (d) $k_{12} = 1.3$. (e) and (f) $k_{12} = 2$.

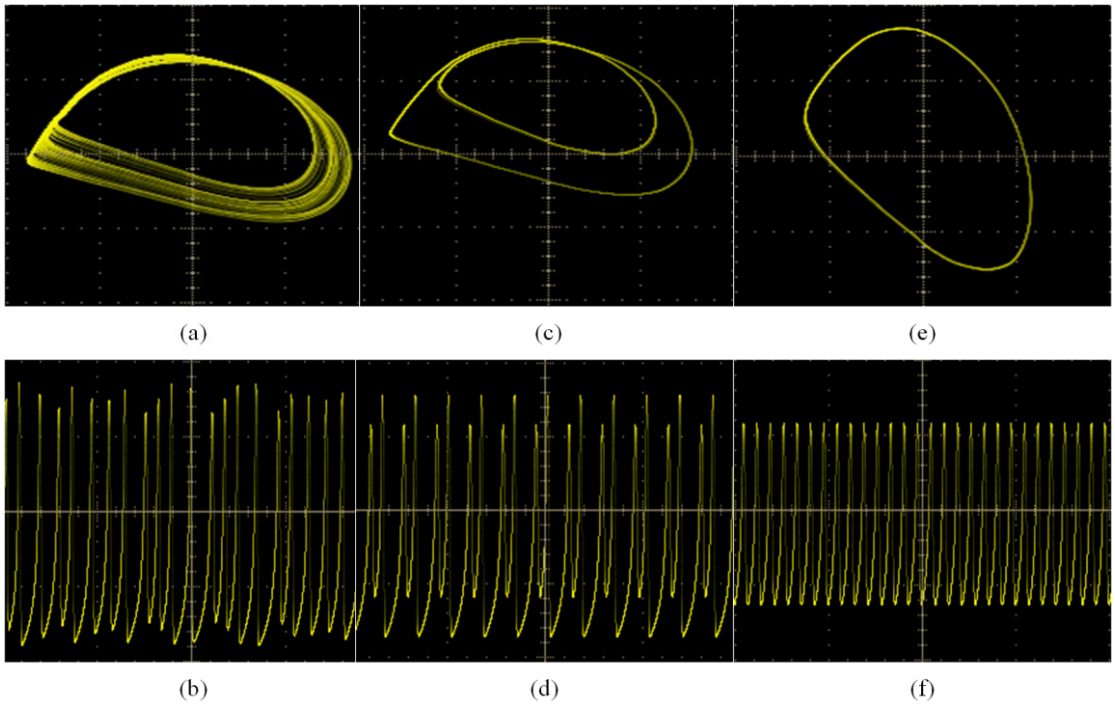


Fig.15. Experimental time series and phase portraits obtained from the DSP platform for different values of k_{23}, with k_{12}=0.1 and k_{31}=1 fixed. The upper panels show phase portraits in the x–y plane, and the lower panels show the corresponding time series of $x(t)$. (a) and (b) k_{23} = 0.5. (c) and (d) k_{23} =1. (e) and (f) k_{23} = 1.5.

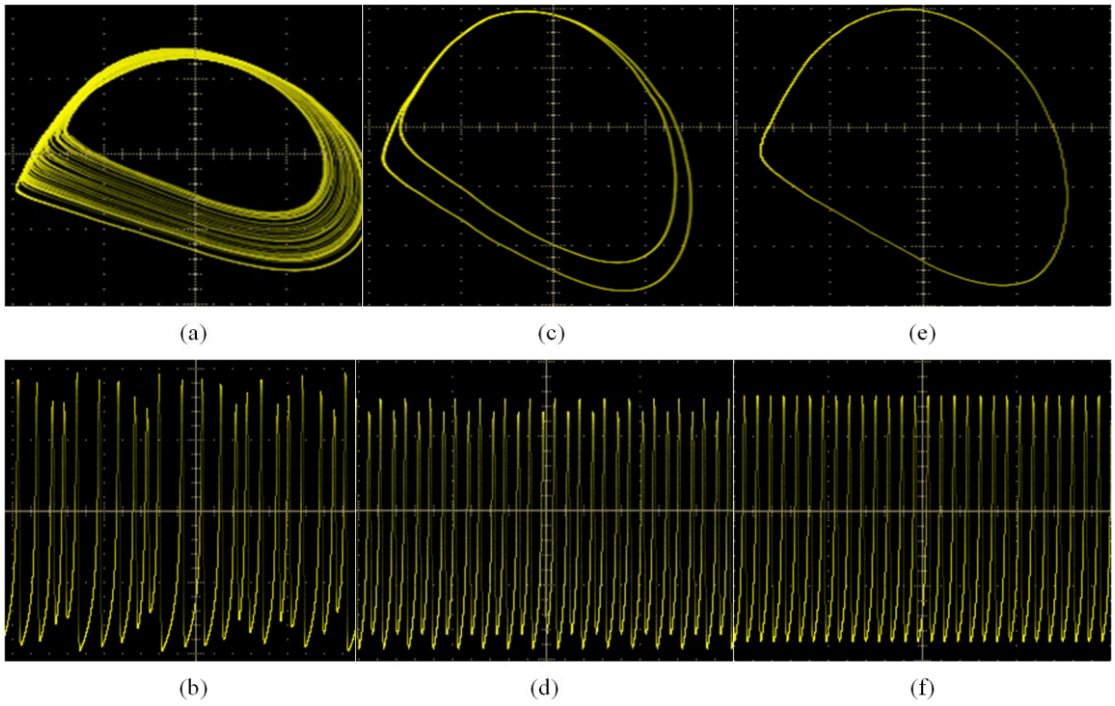


Fig.16. Experimental time series and phase portraits obtained from the DSP platform for different values of k_{31}, with k_{12} = 1.2 and k_{23} = 0.5 fixed. The upper panels show phase portraits in the x–y plane, and the lower panels show the corresponding time series of $x(t)$. (a) and (b) k_{31} = 0.3. (c) and (d) k_{31} = 0.43. (e) and (f) k_{31} = 0.5.

6. Conclusion

This work develops a three-neuron HR ring network equipped with bidirectional third-neuron-mediated gated memristive coupling inspired by tripartite synapses. Unlike constant synaptic weights, the interaction between each pair of neurons is determined by a time-varying effective coupling strength, which is controlled by the membrane potential of a third neuron. This provides an additional regulatory pathway for controlling inter-neuronal interactions while maintaining bidirectional information exchange within the coupling channels. Comprehensive nonlinear dynamical analyses, including bifurcation diagrams, Lyapunov spectra, phase portraits, and two-parameter maps, reveal diverse transitions among periodic, multi-periodic, and chaotic firing states. The three coupling channels exhibit distinct regulatory effects, where k_{12}, k_{23}, and k_{31} collaboratively determine the dynamical evolution of the network. Furthermore, external excitation analysis demonstrates that neuronal inputs provide an additional regulatory pathway by indirectly modulating effective coupling strengths through the third-neuron-mediated gating mechanism. ATMS320F28335 DSP platform is established to physically implement the network. Oscilloscope-measured phase trajectories and time series match numerical simulations well, with small discrepancies only from hardware noise and DAC quantization. The hardware tests validate the discrete solving algorithm and prove the proposed memristive network is hardware-realizable.

Compared with representative tripartite-synapse neural network models, the proposed framework provides a relatively compact and hardware-oriented approach to astrocyte-inspired synaptic regulation. As summarized in Table 2, conventional tripartite-synapse models generally represent astrocytic modulation through explicit astrocyte-related variables and calcium dynamics, whereas the proposed framework uses a third neuron as a functional abstraction of astrocytic regulation without introducing explicit calcium-kinetic equations. In the proposed model, the internal state variable captures the history-dependent modulation of synaptic efficacy, thereby realizing state-dependent synaptic regulation through the gated memristive coupling. In addition, unlike the representative models summarized in Table 2, the proposed framework has been implemented in real time on a DSP platform, demonstrating its hardware feasibility. These characteristics provide a compact and hardware-friendly framework for investigating astrocyte-inspired adaptive neural dynamics and neuromorphic computing.

Table 2. Comparison of the proposed framework with conventional tripartite-synapse models

Ref.	Neuronal model	Astrocyte representation	Calcium dynamics	Model complexity	Hardware platform
[13]	Spiking	Explicit	Yes	Medium–High	Not reported
[14]	HR + FHN	Explicit	Yes	High	Not reported
[33]	Izhikevich	Explicit	Yes	High	Not reported
This work	**HR**	**Functional abstraction**	**No**	**Low**	**DSP**

Notes: “Model complexity” is evaluated by model dimension, presence of calcium dynamics, parameter count, and computational cost.

Declaration of Competing Interest:

The authors declare that they have no known competing financial interests or personal relationships that could have appeared to influence the work reported in this paper.

Funding Statement
This research was funded by the Key Research Project of the Department of Education of Hunan Province (Grant No. 25A0146) and the Research Foundation of Education Department of Hunan Province, China (Grant No. 24A0124).

References

[1] Buzsáki G and Draguhn A 2004 Neuronal Oscillations in Cortical Networks *Science* **304** 1926–9

[2] Chialvo D R 2010 Emergent complex neural dynamics *Nat. Phys.* **6** 744–50

[3] Ma J and Tang J 2015 A review for dynamics of collective behaviors of network of neurons *Sci. China Technol. Sci.* **58** 2038–45

[4] Krahe R and Gabbiani F 2004 Burst firing in sensory systems *Nat. Rev. Neurosci.* **5** 13–23

[5] Mondal A, Upadhyay R K, Ma J, Yadav B K, Sharma S K and Mondal A 2019 Bifurcation analysis and diverse firing activities of a modified excitable neuron model *Cogn. Neurodyn.* **13** 393–407

[6] Yao Z and Wang C 2021 Control the collective behaviors in a functional neural network *Chaos Solitons Fractals* **152** 111361

[7] Dmitrichev A S, Kasatkin D V, Klinshov V V, Kirillov S Y, Maslennikov O V, Shapin D and Nekorkin V I 2018 Nonlinear dynamical models of neurons *Izv. VUZ Appl. Nonlinear Dyn.* **26** 5–58

[8] Lakshmanan S, Lim C P, Nahavandi S, Prakash M and Balasubramaniam P 2016 Dynamical analysis of the Hindmarsh–Rose neuron with time delays *IEEE Trans. Neural Netw. Learn. Syst.* **28** 1953–8

[9] Li Y and Jiang F 2024 Firing activities in a second-order memristor-based Hindmarsh-Rose neuron *Chin. J. Phys.* **89** 1102–15

[10] Korkmaz N, Öztürk İ and Kılıç R 2016 The investigation of chemical coupling in a HR neuron model with reconfigurable implementations *Nonlinear Dyn.* **86** 1841–54

[11] Wang H, Zheng Y and Lu Q 2017 Stability and bifurcation analysis in the coupled HR neurons with delayed synaptic connection *Nonlinear Dyn.* **88** 2091–100

[12] Lin H, Wang C, Deng Q, Xu C, Deng Z and Zhou C 2021 Review on chaotic dynamics of memristive neuron and neural network *Nonlinear Dyn.* **106** 959–73

[13] Stasenko S V, Mikhaylov A N, Fedotov A A, Smirnov V A and Kazantsev V B 2024 Astrocyte control bursting mode of spiking neuron network with memristor-implemented plasticity *Chaos Solitons Fractals* **181** 114648

[14] Chen K and Li Z 2024 Astrocyte mediated firing activities and synchronization in a heterogeneous neuronal network *Chaos Solitons Fractals* **188** 115564

[15] Agulhon C, Petravicz J, McMullen A B, Sweger E J, Minton S K, Taves S R, Casper K B, Fiacco T A and McCarthy K D 2008 What is the role of astrocyte calcium in neurophysiology? *Neuron* **59** 932–46

[16] Chua L 1971 Memristor-the missing circuit element *IEEE Trans. Circuit Theory* **18** 507–19

[17] Strukov D B, Snider G S, Stewart D R and Williams R S 2008 The missing memristor found *nature* **453** 80–3

[18] Wan J, Wu F, Ma J and Wang W 2024 Dynamics and synchronization of neural models with memristive membranes under energy coupling *Chin. Phys. B* **33** 050504

[19] Bao H, Hu A, Liu W and Bao B 2019 Hidden bursting firings and bifurcation mechanisms in memristive neuron model with threshold electromagnetic induction *IEEE Trans. Neural Netw. Learn. Syst.* **31** 502–11

[20] Zhang J and Li Z 2024 Switchable memristor-based Hindmarsh-Rose neuron under electromagnetic radiation *Nonlinear Dyn.* **112** 6647–62

[21] Meng K, Bu Y, Cao Y, Gao S, Li Q, Wang C and Mou J 2026 Chaotic bursting and burst synchronization in a discrete dual-Rulkov neural network with memristive synaptic coupling *Chin. Phys. B* **35** 060501

[22] Bao H, Yu X, Zhang Y, Liu X and Chen M 2023 Initial condition-offset regulating synchronous dynamics and energy diversity in a memristor-coupled network of memristive HR neurons *Chaos Solitons Fractals* **177** 114167

[23] Han B, Liu W and Hu A 2019 Coexisting multiple firing patterns in two adjacent neurons coupled by memristive electromagnetic induction *Nonlinear Dyn.* **95** 43–56

[24] Hajian D N, Ramadoss J, Natiq H, Parastesh F, Rajagopal K and Jafari S 2024 Dynamics of Hindmarsh–Rose neurons connected via adaptive memristive synapse *Chin. J. Phys.* **87** 311–29

[25] Li R, Wang Z and Dong E 2021 A new locally active memristive synapse-coupled neuron model *Nonlinear Dyn.* **104** 4459–75

[26] Chua L 2019 If It's Pinched It's a Memristor *Handbook of Memristor Networks* ed L Chua, G Ch Sirakoulis and A Adamatzky (Cham: Springer International Publishing) pp 15–88

[27] Hindmarsh J L and Rose R M 1982 A model of the nerve impulse using two first-order differential equations *Nature* **296** 162–4

[28] Perea G, Navarrete M and Araque A 2009 Tripartite synapses: astrocytes process and control synaptic information *Trends Neurosci.* **32** 421–31

[29] Noriega-Prieto J A and Araque A 2021 Sensing and Regulating Synaptic Activity by Astrocytes at Tripartite Synapse *Neurochem. Res.* **46** 2580–5

[30] Wolf A, Swift J B, Swinney H L and Vastano J A 1985 Determining Lyapunov exponents from a time series *Phys. Nonlinear Phenom.* **16** 285–317

[31] Mou J, Cao H, Zhou N and Cao Y 2024 An FHN-HR neuron network coupled with a novel locally active memristor and its DSP implementation *IEEE Trans. Cybern.* **54** 7333–42

[32] Yang X-B, He Y-G, Li C-L and Liu C-Q 2020 Analysis, Stabilization, and DSP-Based Implementation of a Chaotic System with Nonhyperbolic Equilibrium *Complexity* **2020** 1–11

[33] Sajedinia Z and Hélie S 2018 A New Computational Model for Astrocytes and Their Role in Biologically Realistic Neural Networks *Comput. Intell. Neurosci.* **2018** 1–10